

# Investigation of Real-Time Microstructure Evolution in Steep Thermal Gradients Using in-Situ Spatially Resolved X-ray Diffraction: A Case Study for Ti Fusion Welds

Thorsten Ressler, Joe Wong,\* and John W. Elmer

Lawrence Livermore National Laboratory, University of California, P.O. Box 808,  
Livermore, California 94551

Received: July 16, 1998; In Final Form: October 5, 1998

A recently developed spatially resolved X-ray diffraction (SRXRD) technique utilizing intense synchrotron radiation has been refined to yield phase and microstructural information down to 200  $\mu\text{m}$  in spatial extent in materials subjected to steep thermal gradients during processing. This SRXRD technique has been applied to map completely the phases and their solid-state transformation in the so-called heat-affected zone (HAZ) in titanium fusion welds in situ during the welding process. Detailed profile analysis of the SRXRD patterns revealed four principal microstructural regions *at temperature* in the vicinity of the HAZ surrounding the liquid weld pool: (i) a completely transformed  $\beta$ -Ti zone 2–3 mm adjacent to the liquid weld pool; (ii) a mixed  $\alpha$ + $\beta$ -Ti region surrounding the pure  $\beta$ -Ti zone, (iii) a back-transformed  $\alpha$ -Ti zone on the backside of the HAZ where pure  $\beta$ -Ti once existed at temperature well above the  $\alpha \rightarrow \beta$  transformation isotherm, and (iv) a more diffused region outside the HAZ where annealing and recrystallization of the  $\alpha$ -Ti base metal occur. The high-temperature microstructures so derived corroborate well the expected transformation kinetics in pure titanium, and the observed phase transformation boundaries are in good agreement with those predicted from the transformation isotherms calculated from a simplified heat-flow model. Based on a detailed assessment of the SRXRD setup employed, improved experimentations such as a smaller beam spot emitted from third generation synchrotron sources, better mechanical stability (tighter scattering geometry), and use of an area detector would enable more quantitative structural information for future phase dynamics studies exemplified by this work.

## Introduction

Real-time studies of dynamical processes in situ under severe temperature or pressure conditions often pose a challenge for experimentalists. In materials synthesis (such as combustion synthesis) and materials joining processes (such as welding), high-intensity heat sources are used to create steep thermal gradients that rapidly heat and cool materials to and from their melting point. This rapid thermal cycling induces solid-state reactions and/or phase transformations both on heating and on cooling and causes melting and solidification in regions of the material where the liquidus temperature has been exceeded. Composition and/or structure fluctuations are expected to occur along thermal gradients, and microstructural discontinuities exist at (or near) the location of each phase transformation isotherm.

Materials systems where thermally induced phase transformations play a significant role include allotropic elements such as pure titanium ( $\text{hcp} \rightarrow \text{bcc}$ ), two-phase alloys such as stainless steels ( $\text{fcc} \rightarrow \text{bcc}$ ), martensitic alloys such as iron-based steel alloys ( $\text{fcc} \rightarrow \text{bct}$ ), and dispersion-strengthened alloys. Most of the phase transformations of interest will involve deviations from equilibrium microstructures, resulting in partial transformations and/or the creation of metastable phases. These types of phase transformations have aroused a lot of interest in recent years in welding research development and in the metallurgical community.<sup>1</sup>

From a practical standpoint, solid-state phase transformations and their kinetics play an important role in understanding various

problems associated with thermal processing of materials such as subsolidus cracking, cold cracking, and distortion caused by residual stresses.<sup>2,3</sup> Solution to these problems will greatly be facilitated by the development of novel experimental methods for determining phase transformation behavior in the steep thermal gradients and at the high cooling rates. Currently, there are only a handful of in-situ, real-time studies of phase changes and chemical dynamics mostly carried out in high-temperature reaction systems involving solid combustion.<sup>4–7</sup> Until recently,<sup>8</sup> no direct method exists for investigating solid-state phase transformations that take place. Conventional methods for studying general phase transformation behavior are mostly *indirect* and of a *post-mortem* nature. Moreover, these methods only provide data for low heating and cooling rates on the order of  $\sim 1$  K/s, which is much less than those of arc welds ( $10$ – $10^3$  K/s) and laser and electron beam welds ( $10^2$ – $10^4$  K/s).

Recently, we have developed a spatially resolved X-ray diffraction (SRXRD) technique using intense synchrotron radiation to probe the phases and map their locations in steep thermal gradients down to 200  $\mu\text{m}$  in spatial extent in situ, in real time and at temperature during the welding process.<sup>8,9</sup> In a fusion weld, two distinct microstructural regions are formed: (i) the *fusion zone*, FZ, in which melting, solidification, and solid-state phase transformation have taken place, and (ii) the *heat-affected zone*, HAZ, in which only solid-state phase transformations have taken place. In each zone, metastable microstructures may be created that can enhance or degrade the quality of the weld, depending on the materials and processing parameters.

In this paper, we choose titanium fusion welds as a case study

\* Corresponding author. e-mail wong@cms1.llnl.gov, FAX (925) 422 2118, phone (925) 423 6385.

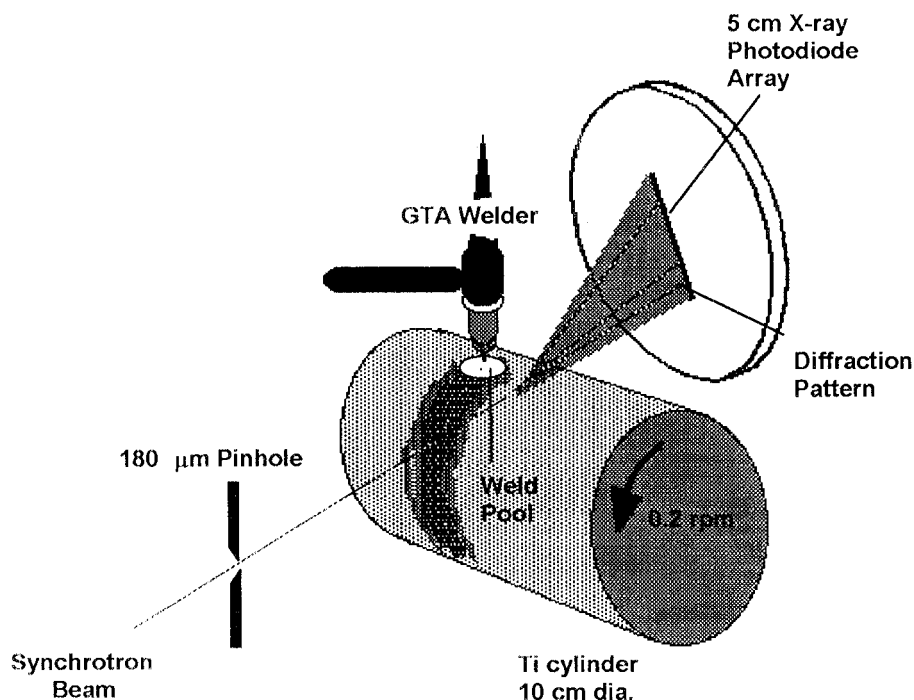


**Figure 1.** Schematics of the SRXRD setup used for in-situ phase mapping and real-time observation of microstructure evolution in fusion welds.<sup>9</sup>

and apply our SRXRD technique to map completely the phases and their solid-state transformations in the HAZ in situ during the welding process. Results of profile analysis of the diffraction data were used to elucidate the evolution of various types of high-temperature microstructures in the vicinity of the HAZ surrounding the liquid weld pool. The observed phase boundaries are compared with those calculated from a heat-flow model. The diffraction geometry used in this study will be described in some detail. Improved experimentation for future in-situ phase dynamics investigations exemplified by this work is also given.

### Experimental Section

**Titanium.** Cylindrical welding samples were machined from as-received grade 2 commercially pure titanium measuring 10.2 cm in diameter and 12.7 cm in length. These samples had a surface finish of 1.6 μm rms and were round to within 10 μm on the diameter. Chemical analysis was performed using combustion analysis for O, C, N, and H and inductively coupled plasma analysis for the remaining elements. The results show the following impurity content (weight percent): 0.14% Fe, 0.17% O, 0.03% Al, 0.02% Cr, 0.008% C, 0.001% H, 0.014% N, 0.02% Ni, 0.005% V, and 0.004% Si. The final cylindrical samples were then vacuum-annealed for 30 min at 400 °C to partially recover from the cold work that was introduced during machining.

**Welding.** Gas tungsten arc welds were made on the titanium bars using a 150 A direct current welding power supply with the electrode held at negative polarity. A new welding electrode made of W-2% Th, 4.7 mm in diameter, was used for each weld. The power was maintained constant at 1.9 kW (100 A, 19 ± 0.5 V) for all welds, and helium was used as both a welding and shielding gas. The titanium bar was rotated at a constant speed of 0.20 rpm below the fixed electrode, which corresponds to a surface welding speed of 1.1 mm/s. These conditions resulted in an 11–12 mm wide fusion zone on the surface of the titanium bar. All welding was performed inside a chamber purged with ultrahigh-purity helium (99.999%) to

minimize oxidation of the titanium that had occurred.<sup>9</sup> The He gas was also passed through the torch during welding to further prevent oxidation in the weld region and to cool the torch. The welding assembly was integrally mounted to a translation stage driven by a stepper motor with 10 μm precision. Spatial mapping of the phases in the various regions of the HAZ was performed by using the translation stage to manipulate the weld (welding torch and workpiece) with respect to the fixed X-ray beam in order to sample discrete regions around the weld. Movements perpendicular to the centerline of the weld were controlled by a computer and were performed by direct translation of the workpiece with respect to the X-ray beam. An in-house designed software package was developed on a personal computer using LabView software v4.0 to control the position of the weld with respect to the X-ray beam, to control the bar rotational speed (welding speed), and to trigger the data acquisition system in a second computer.

**Spatially Resolved X-ray Diffraction (SRXRD).** SRXRD experiments were performed on the 31-pole-wiggler beam line 10-2<sup>10</sup> at Stanford Synchrotron Radiation Laboratory (SSRL) with the storage ring operating at an electron energy of 3.0 GeV and injection current of ~100 mA. Details of the SRXRD instrument can be found in refs 8 and 9. A schematic representation of the experimental setup is shown in Figure 1.

XRD measurements were made using a monochromatic X-ray beam with a photon energy of 8.5 keV (wavelength  $\lambda = 1.4586$  Å). A Si(111) double-crystal monochromator was used preceded by a toroidal mirror in a 1:1 focusing geometry. The spatial resolution of the experiment was determined by a 180 μm pinhole placed 30 cm in front of the weld. A photon flux of about  $2 \times 10^9$  photons/s was determined using an ionization chamber situated between pinhole and weld. From photographic paper measurements the beam size on the titanium bar was estimated to be ~200 μm. X-ray diffraction patterns from the titanium bar were recorded on a Peltier-cooled 5 cm long, 2048 elements position sensitive photodiode array detector. The detector was placed 9.5 cm from the weld at an angle of ~30° with respect to the primary synchrotron beam covering a  $2\theta$

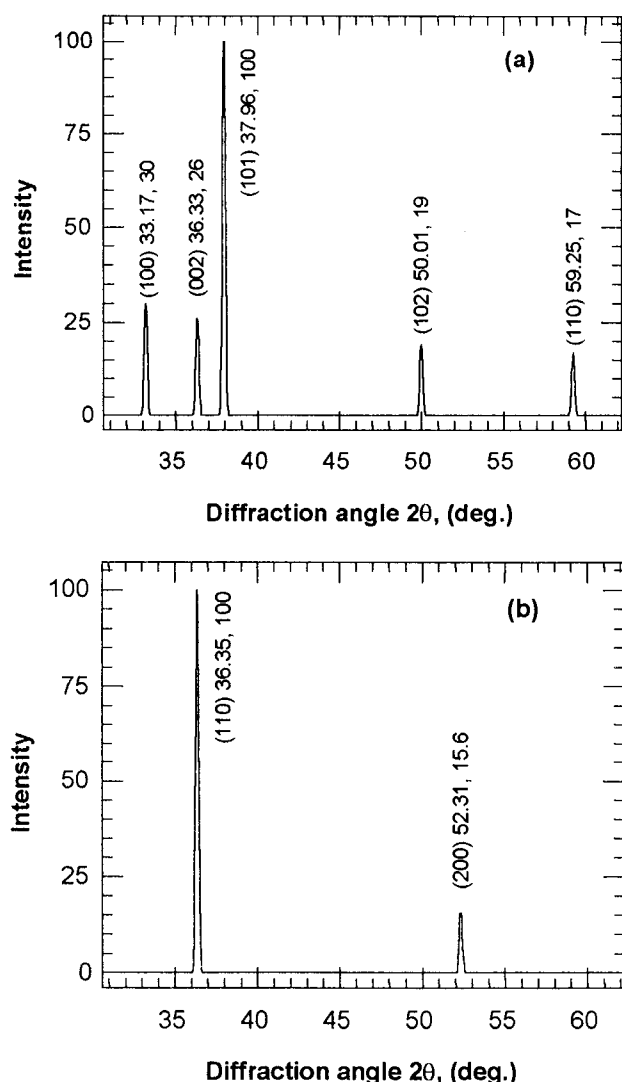


**Figure 2.** Calculated<sup>16</sup> powder X-ray diffraction patterns for (a)  $\alpha$ -Ti hcp,  $a = 2.9503$  Å,  $c = 4.6810$  Å at 25 °C<sup>17</sup> and (b)  $\beta$ -Ti bcc,  $a = 3.3112$  Å at 920 °C,<sup>17</sup> in the experimental  $2\theta$  window at a photon energy of 8.5 keV ( $\lambda = 1.4586$  Å). Indicated are  $(hkl)$  indices, peak position, and relative intensity. Line shape results from convolution with an arbitrary instrumental function. The line width was chosen to match experimental base metal  $\alpha$ -Ti diffraction peaks.

range from 30° to 60°. Figure 2 shows calculated powder X-ray diffraction patterns for the two principal titanium phases ( $\alpha$ -Ti and  $\beta$ -Ti) in this  $2\theta$  range. The detector and associated ST121 data acquisition system were manufactured by Princeton Instruments.<sup>11</sup> The latter was used to store and display the X-ray diffraction data in real time.

SRXRD patterns were measured during welding by positioning the beam at a predetermined location with respect to the welding electrode. A single diffraction pattern at each location was collected for 6 s while the bar rotated under the torch at a constant speed of 0.2 rpm. By incrementally jogging the weld to new locations in 200  $\mu$ m intervals, a series of spatially resolved X-ray diffraction patterns were collected along a lineal scan direction perpendicular to and away from the centerline of the weld. For example, a typical run consisted of gathering 40 X-ray diffraction patterns spanning a range of 8 mm through the HAZ. A schematic representation of the mapping procedure is presented in Figure 3. The dimension of the liquid weld pool was determined from the experiment, whereas the dimension of the heat-affected zone was estimated from a heat-flow model.<sup>12</sup> Each dotted line represents a single experimental

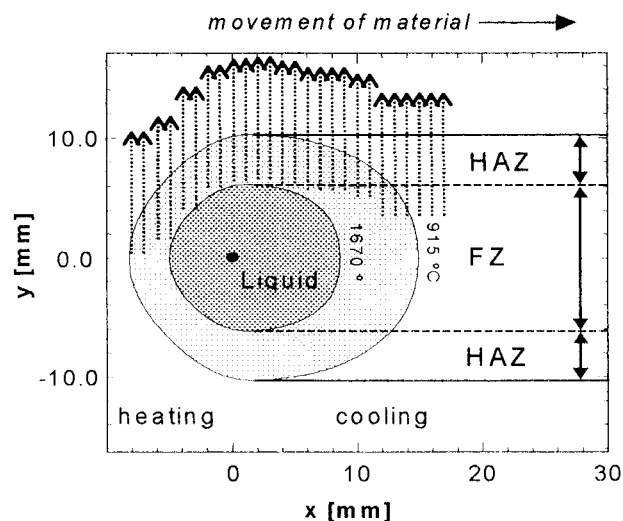


**Figure 3.** Schematic representation of the SRXRD procedure used. Indicated are HAZ (limited by 915 °C isotherm) and FZ (limited by 1670 °C isotherm) as determined from heat-flow model calculations and the direction of movement of the titanium material underneath the tungsten electrode (black dot at  $x = 0.0$  mm and  $y = 0.0$  mm). Each dotted arrow represents a single experimental SRXRD run, and each dot denotes an X-ray diffraction pattern measured at that location. Heating and cooling side of the moving weld are indicated.

SRXRD run, and each dot denotes an X-ray diffraction pattern collected at this location with respect to the center of the weld. After completing a run, the weld was allowed to cool to room temperature, and the electrode was repositioned to a new starting location with respect to the X-ray beam prior to taking the next series of data. As can be seen from Figure 3, by symmetry only one-half the weld was mapped experimentally. In the following analysis, only the top half of the entire weld will be displayed for simplicity.

**Data Analysis.** The X-ray diffraction data were analyzed using the WinXAS software package.<sup>13</sup> Conversion from photodiode number to  $2\theta$  angle was performed by linearly fitting experimental  $(hkl)$  peak positions (in pixel number) of the  $\alpha$ -Ti room-temperature diffraction pattern taken prior to each SRXRD run to the corresponding  $(hkl)$  peak position (in  $2\theta$ ) of the calculated  $\alpha$ -Ti pattern at the same wavelength (Figure 2). Single or multiple diffraction peaks in the SRXRD data were fitted with a sum of one or more Gaussian profile functions and a linear background using a standard least-squares refinement procedure. Due to the limited number of data points in multiple-peak diffraction lines, the fwhm (full width at half-maximum) of the respective Gaussian functions were refined to vary the same. Multiple scan data in each SRXRD file were analyzed in a serial procedure employing the macro capabilities of WinXAS.

**Error Estimates.** Three distinguishable types of error are relevant to this work: (i) error in spatial disposition of different phases in the map, (ii) error in the SRXRD peak positions, and (iii) error in the SRXRD peak widths. The latter two are largely due to geometric effects arising from the employed diffraction setup.

**Spatial Error.** The error arises from a contribution of uncertainty in locating the X-ray beam with respect to the center of the weld, motion of the weld pool about its center, and fluctuation in the weld pool size. Using X-ray photographic paper and a gauge scale with 0.5 mm marks, the uncertainty in positioning the weld electrode was estimated to be  $\pm 0.25$  mm. Side-to-side motions perpendicular to the weld direction contributed a further uncertainty of  $\pm 0.25$  mm indicated by



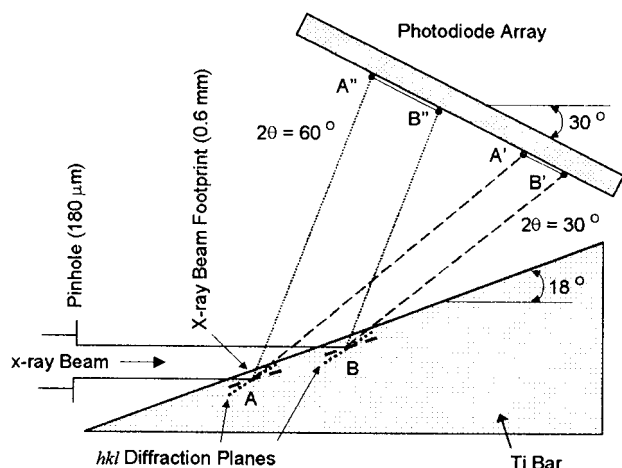


**Figure 4.** Schematic representation of the scattering geometry used. The height of the X-ray beam is determined by a  $180\text{ }\mu\text{m}$  pinhole, and the X-ray illuminated surface of the Ti bar can be assumed to be flat. The footprint on sample, AB, along the beam direction amounts to  $\sim 0.6\text{ mm}$ . Two sets of  $hkl$  diffraction planes (dashed with  $\theta = 15^\circ$  and dotted with  $\theta = 30^\circ$ ) at locations A and B represent domains fulfilling Bragg's law and resulting in diffracted beams with  $2\theta = 30^\circ$  and  $2\theta = 60^\circ$ . Distances  $A'B'$  and  $A''B''$  depict line broadening (for many domains) or splitting (for only a few domains) of the corresponding ( $hkl$ ) peaks on the photodiode array (note that  $A''B'' > A'B'$  with increasing  $2\theta$ ).

postweld photographs. Variations in weld pool width from start to finish of a given welding run add a further spatial uncertainty of  $\pm 0.5\text{ mm}$ . These three sources of error yield an overall error of  $\pm 1.0\text{ mm}$  to the spatial location of the observed phases in the resultant map.

**Error in SRXRD Peak Position.** The diffraction geometry shown in Figure 1 is naturally sensitive to changes in the vertical position of the Ti bar with respect to the X-ray beam during the SRXRD measurement. A slight misalignment of the metal bar with respect to the diffraction plane results in a wobbling motion horizontally and vertically. The amplitude of these displacements increases with increasing distance of the weld from the mounting support and may vary from bar to bar. The peak shifts recorded on the photodiode array resulting from the wobbling motion are found to be in the same order of magnitude as those calculated for thermal expansion of the material. This renders quantitative evaluation of lattice parameters and thermal expansion coefficient from peak position difficult. In addition, vertical wobbling alters the size of the beam footprint on the Ti bar which can result in changing peak intensities. This problem may be obviated using stationary spot-welds associated with a time-resolved diffraction procedure as has been applied successfully with combustion synthesis reactions.<sup>6</sup>

**Error in Width of SRXRD Peaks.** This source of error arises from the projection (footprint) of the X-ray beam on the titanium bar as illustrated in Figure 4. The beam footprint on the Ti surface (distance AB in Figure 4) yields a peak broadening due to diffraction domains fulfilling Bragg's law at different heights with respect to the center of the X-ray beam (location A and B in Figure 4). For the diffraction geometry shown in Figure 4, this effect results in an increased broadening at higher diffraction angle  $2\theta$  (e.g.,  $A'B' < A''B''$  in Figure 4). This trend is indeed observed in the experimental diffraction data (width of  $\alpha$ -Ti (002)  $<$  (101)  $<$  (102)). When only a few large domains contribute to the measured diffraction lines, the footprint effect can result in a splitting of single diffraction lines into multiple peaks. Such splittings are observed in both  $\alpha$ -Ti (Figure 13) and  $\beta$ -Ti diffraction patterns. Thus, a multiple peak diffraction

line in the experimental data must *not* be taken to indicate the occurrence of separate phases with slightly different lattice parameters, but rather as a scattering geometry effect. Also, the "footprint" peak broadening renders a quantitative analysis of diffraction domain sizes using the Scherrer formula<sup>13</sup> difficult. However, since this effect is smallest for the low-angle lines, their line widths were used to estimate domain sizes and to compare evolution of grain size in different microstructural regions of the weld. Furthermore, assuming a resolution of the photodiode array of about 1.5 diodes ( $\sim 0.02^\circ 2\theta$  in the current geometry), as specified by the manufacturer, a peak width of one diode numerically corresponds to a diffraction domain size of about  $0.5\text{ }\mu\text{m}$  from the (002) line. Larger domains will not necessarily result in narrower peaks and hence may not be distinguished with the diffraction setup used for this work.

## Results

Pure titanium exhibits two phase transitions: an  $\alpha \rightarrow \beta$  phase transformation in the solid state at  $882^\circ\text{C}$  and melting at  $1668^\circ\text{C}$ .<sup>15</sup> In commercially pure grade 2 titanium employed in this work, the allotropic transformation from a hcp  $\alpha$ -phase to a bcc  $\beta$ -phase occurs at  $\sim 915^\circ\text{C}$  due to the presence of iron, oxygen, and other impurities.<sup>15</sup> During the welding process, these phase transitions give rise to two distinct microstructural regions: a fusion zone (FZ), in which melting upon heating and solidification on cooling occur, and a heat-affected zone (HAZ), in which the  $\alpha \rightarrow \beta$  solid-state phase transformation and other microstructural changes take place. A typical series of SRXRD patterns measured across the  $\alpha \rightarrow \beta$  phase transformation isotherm are shown in Figure 5. The starting position and scan direction of the SRXRD run with respect to the center of the weld are shown by the dotted arrow in the inset. A transition from a  $\beta$ -Ti bcc pattern at high-temperature inside the HAZ to a  $\alpha + \beta$ -mixed zone, and eventually to the  $\alpha$ -Ti hcp pattern, can be seen. In addition to phase transformations, the material undergoes annealing and recrystallization in the cooler region and outside the HAZ. SRXRD data obtained from different starting positions with respect to the weld center may be classified into five principal diffraction patterns. Examples for each of the principal patterns are displayed in Figure 6 together with one for the  $\alpha + \beta$ -coexistence region. These principal diffraction patterns are described as follows:

**The  $\alpha$  Pattern.** This pattern corresponds to the base metal  $\alpha$ -Ti phase at ambient temperature prior to welding. Compared to the calculated powder diffraction pattern for  $\alpha$ -Ti (Figure 2), a strong (002) line and a less intense (101) line can be seen. This indicates a preferred orientation of the hexagonal basal plane parallel to the surface in the Ti bar due to the extrusion processes. The hcp (100) and (110) peaks are invisible on the scale of Figure 6 for the same reason. Finally, a slight asymmetry can be seen on the low  $2\theta$  side of each diffraction peak.

**The  $\alpha_{AR}$  Pattern.** This pattern represents an annealed and recrystallized (hence the subscript AR)  $\alpha$ -Ti phase. On the colder side of the  $915^\circ\text{C}$  isotherm in Figure 5a, the material undergoes annealing and recrystallization. Annealing of  $\alpha$ -Ti is indicated by a decreasing peak width due to reduction in dislocations, stress, and lattice distortions in the  $\alpha$ -Ti base metal. A thin layer of surface titanium oxide intrinsic to the base metal gives rise to a  $\text{TiO}_x$  shoulder on the low-angle side of each hcp diffraction peak. The appearance of  $\text{TiO}_x$  in Ti welds has been reported and analyzed in some detail earlier.<sup>9</sup> However, the concentration and therefore height of the  $\text{TiO}_x$  shoulder in the

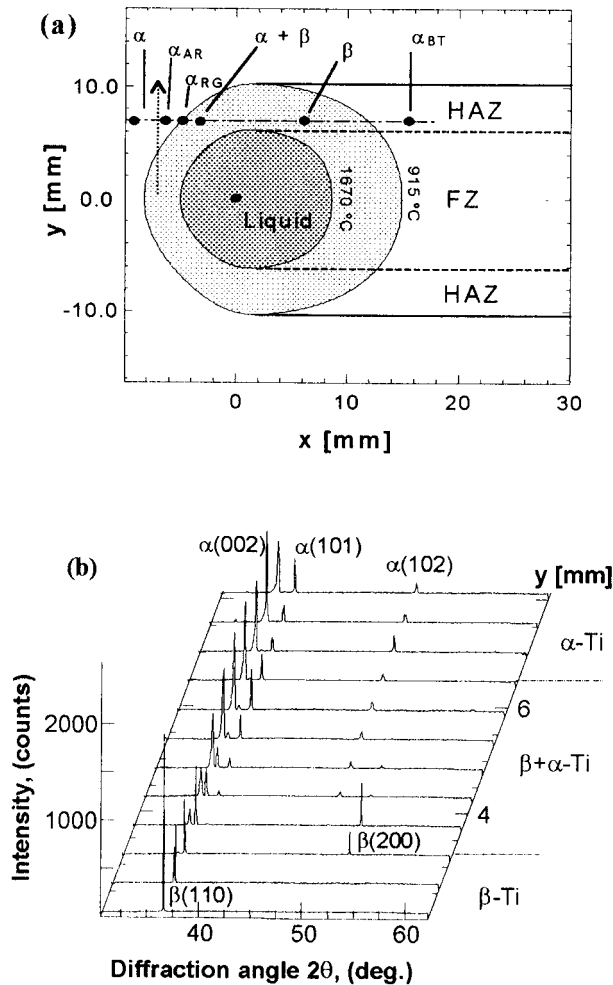


**Figure 5.** A series of SRXRD patterns measured across the  $\alpha \rightarrow \beta$  phase transformation isotherm ( $T = 915^\circ\text{C}$ ) in the  $y$  direction along the negative temperature gradient at a position  $x = -6$  mm ahead of the center of the weld (dotted arrow in inset) showing the  $\beta$ -Ti,  $\beta + \alpha$  coexistence, and  $\alpha$ -Ti zones.

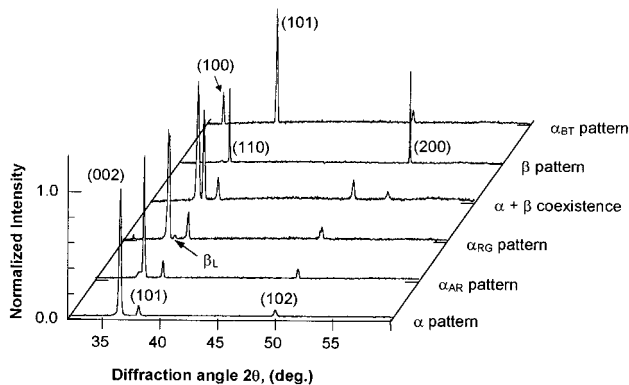


**Figure 6.** Principal diffraction patterns obtained from the current SRXRD measurement on titanium fusion welds. ( $\alpha$ ) represent the base metal hcp  $\alpha$ -Ti phase. ( $\alpha_{AR}$ ) is for the annealed and recrystallized  $\alpha$ -Ti. ( $\alpha_{RG}$ ) denotes a recrystallized  $\alpha$ -Ti phase exhibiting large diffraction domains (grain growth). ( $\alpha_{BT}$ ) is for the back-transformed  $\alpha$ -Ti that forms from the region of the HAZ that once contained  $\beta$ -Ti. ( $\beta$ ) is for the  $\beta$ -Ti phase, and ( $\beta_L$ ) is for the  $\beta$ -Ti that coexists with  $\alpha$ -Ti in low amounts predominantly together with  $\alpha_{BT}$ . The  $z$  axis in the plot represents a line,  $y = 7$  mm parallel to the centerline of the weld as shown in Figure 5a, that would yield this series of six SRXRD patterns. Data were normalized to unity for the highest peak in each pattern.

current data are much lower with the use of the He environmental chamber. A detailed profile analysis revealed that the

**TABLE 1: Characteristics of Various Ti hcp and bcc SRXRD Patterns Observed in the Vicinity of the Heat-Affected Zone of a Ti Fusion Weld**

XRD pattern	preferred orientation	line width [ $2\theta$ , deg]	TiO <sub>x</sub> phase	multiplet
$\alpha_{\text{base metal}}$	hcp (002)	0.22 (002)	yes	no
$\alpha_{AR}$	hcp (002)	0.18 (002)	yes	no
$\alpha_{RG}$	hcp (002)	0.07 (002)	yes	yes
$\beta_L$	bcc (110)	0.23 (110)	no	no
$\beta$	bcc (110)	0.04 (110)	no	yes
$\alpha_{BT}$	hcp (101)	0.16 (002)	no	no

shoulder can be observed on all three diffraction lines, indicating indeed a contribution of the reported TiO<sub>x</sub> phases.

**The  $\alpha_{RG}$  Pattern.** This pattern denotes a recrystallized  $\alpha$ -Ti phase with diffraction domains on the order of a few microns. Due to the scattering geometry employed, this domain size can result in well-resolved multiplets within one diffraction line. As discussed in the section on "Error Estimates", these multiple peaks must not be taken to indicate different phases having different lattice constants. The  $\alpha_{RG}$  patterns also show the TiO<sub>x</sub> shoulder and a low amount of  $\beta$ -Ti which is denoted ( $\beta_L$ ) in Figure 6.

**The  $\alpha_{BT}$  Pattern.** This pattern denotes the  $\alpha$ -Ti phase on the trailing (cooling) side of the weld, back-transformed from regions in the HAZ that once contained  $\beta$ -Ti at high temperature. A preferred orientation in the (101) direction compared to the (002) texture of the base metal can be seen in Figure 6. A residual amount of Ti  $\beta$ -phase occasionally remains in the back-transformed  $\alpha$ -phase. (The ratio of integrated intensity of pure  $\beta$ -phase and residual  $\beta$ -phase is on the order of 10%.)

**The  $\beta$  Pattern.** This pattern corresponds to the high-temperature bcc Ti phase. Figure 6 also displays a diffraction pattern observed in the region of the HAZ where both  $\alpha$ -Ti and  $\beta$ -Ti coexist. Transformation of the (002) textured base metal to  $\beta$ -Ti appears to afford a preferred orientation in the (110) direction of the  $\beta$ -Ti lattice.

It should be emphasized that all principal diffraction patterns belong to either the  $\alpha$ -Ti or the  $\beta$ -Ti phase but indicate differences in texture, degree of recrystallization or annealing, or phase concentration *at temperature and at given location*. The characteristics of the five principal Ti hcp and bcc diffraction patterns and the  $\beta_L$  pattern are summarized in Table 1. The spatial disposition of these five principal X-ray diffraction patterns with respect to the weld center is displayed in Figure 7. The map of the phases existing in the HAZ during welding was assembled from the SRXRD experimental data. Sequential X-ray diffraction runs were analyzed to determine the spatial position of the different patterns along a direction perpendicular to the weld direction. Each scan covered a distance of approximately 8 mm and contained about 40 diffraction patterns. Twenty-one individual scans were made with the first scan situated 8 mm ahead of the weld center, and the last scan was made at a location 20 mm behind the weld center. This span of 28 mm was wide enough to encompass the entire HAZ region under the welding conditions used. When both  $\alpha$ - and  $\beta$ -Ti coexist, two bars are presented side by side. The left and the right bar of each pair represent the presence of  $\alpha$ -Ti and  $\beta$ -Ti, respectively. For many of the runs shown, both bars overlap in  $y$ , indicating zones where both phases coexist during welding. By mirror symmetry only the upper half of the liquid weld pool and the HAZ is displayed.

## Discussion

**Thermal Distribution and General Consideration.** Figure 8 shows a plot of the temperature distribution in the titanium

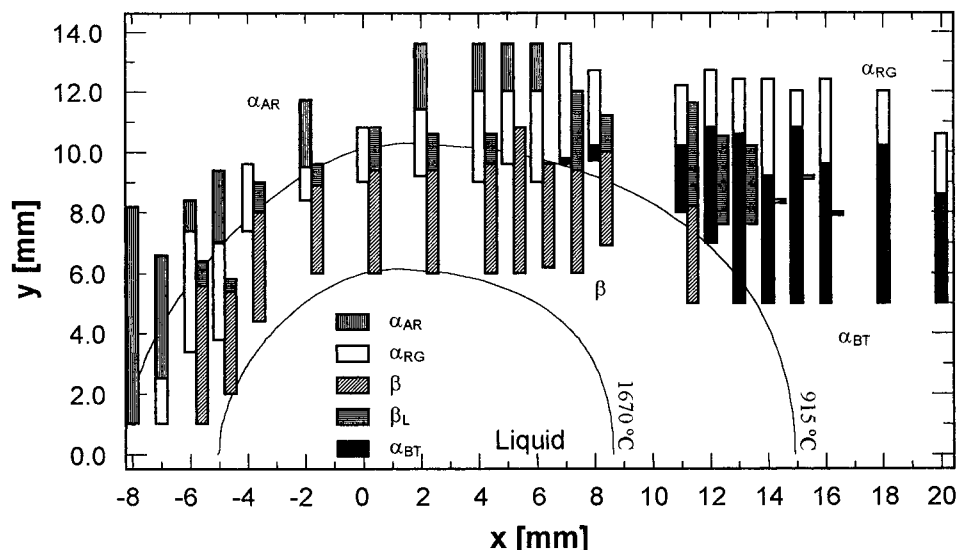


**Figure 7.** SRXRD map presenting the locations of four principal diffraction patterns plus  $\beta_L$  with respect to the HAZ of the weld. A total of 21 individual scans are displayed together with two calculated weld isotherms. For scans presented by two bars side by side, the left bar represents the presence of  $\alpha$ -Ti and the right bar for  $\beta$ -Ti. Each bar again is subdivided into regions with different shadings to indicate the different types of diffraction patterns that were present: ( $\alpha_{AR}$ ) is the annealed and recrystallized  $\alpha$ -Ti; ( $\alpha_{RG}$ ) denotes a recrystallized  $\alpha$ -Ti phase which exhibits large diffraction domains; ( $\alpha_{BT}$ ) is the back-transformed  $\alpha$ -Ti that forms from the region of the HAZ that once contained  $\beta$ -Ti; ( $\beta$ ) is the  $\beta$ -Ti phase; ( $\beta_L$ ) is the  $\beta$ -Ti that coexists with  $\alpha$ -Ti in low amounts predominantly together with  $\alpha_{BT}$ . The  $\alpha$  pattern is not shown in this phase map since the SRXRD data were not recorded far enough into the cold region of the HAZ.

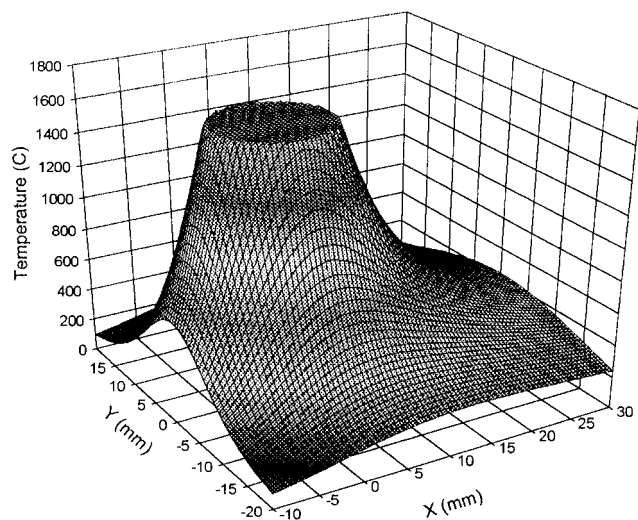


**Figure 8.** Temperature distribution for a 1.9 kV titanium fusion weld as calculated from a simplified heat-flow model.<sup>8,12</sup>

fusion weld studied in this work. The display has been capped at a temperature of 1670 °C, the melting temperature of Ti, with the resulting plateau representing the weld liquid pool. Temperature data were calculated from a simplified heat-flow model taking into account welding and thermal parameters such as travel speed of Ti bar, voltage and current used, integration time per data point, and thermal conductivity. Subsequently, the heat-flow model was refined using the experimental dimension of the liquid weld pool and the SRXRD data. Details about the heat-flow model calculation are reported elsewhere.<sup>8,12</sup>

A steep temperature gradient on the order of 100 K/mm occurs on the front (heating) side of the weld, whereas behind the weld (cooling side) a smoother descent in temperature is evident. The difference in thermal gradient is expected to reflect differences in the microstructural evolution in the heat-affected zone around the liquid weld pool. To understand phase transformation and changes in the microstructure, the phase map around the Ti weld given in Figure 7 has to be examined in

both the  $x$  and  $y$  directions. Situated ahead of the weld (negative  $x$  direction) and parallel to the welding direction is the heating zone with a steep positive thermal gradient toward the center of the weld pool. Further down from the center of the liquid pool (positive  $x$  direction) is the cooling zone parallel to the welding direction. Moving out from any  $x$  position toward increasing positive  $y$  is the cooling zone perpendicular to the welding direction. Moreover, the dynamic character of weld under these particular conditions should be realized. For example, titanium base metal is only present ahead of the liquid pool in the  $x$  direction and far out from the weld center at any  $y$  position. The  $\alpha$ -Ti phase in a direct line behind the liquid pool has first undergone a complete  $\alpha \rightarrow \beta$  phase transformation and then  $\beta \rightarrow \alpha$  back-transformation. In a simplified scheme,  $\alpha$ -Ti above a line drawn from the maximum of the phase transformation isotherm (915 °C, Figure 7) parallel to  $x$  has never been transformed to  $\beta$ -Ti but may undergo microstructural changes. Furthermore,  $\alpha$ -Ti behind the coexistence region in the map and outside the 915 °C isotherm has to be regarded as consisting of a mixture of back-transformed  $\alpha$ -Ti and annealed and recrystallized but not transformed  $\alpha$ -Ti. The observed SRXRD patterns have to reflect these changes in the welded material. In the following, the five principal diffraction patterns will be discussed in detail and correlated with the associated microstructure at various locations in the HAZ and its vicinity during the welding process.

**The  $\alpha_{AR}$  Pattern: Location and Associated Microstructure.** The locations at which the  $\alpha_{AR}$  pattern was observed are plotted in Figure 9a. The corresponding diffraction pattern is shown in Figure 9b. Profile analysis revealed that the peak width of the  $\alpha_{AR}$  patterns appearing at the end of each of the SRXRD scans (Figure 7) was narrower than the room-temperature base metal peak width. This implies that none of the 21 SRXRD scans were measured far enough out to reach the thermally unaffected titanium base metal.

Polycrystalline titanium base metal starts with small diffraction domains and grains that exhibit a high degree of disorder and internal stress due to the extrusion and machining process.



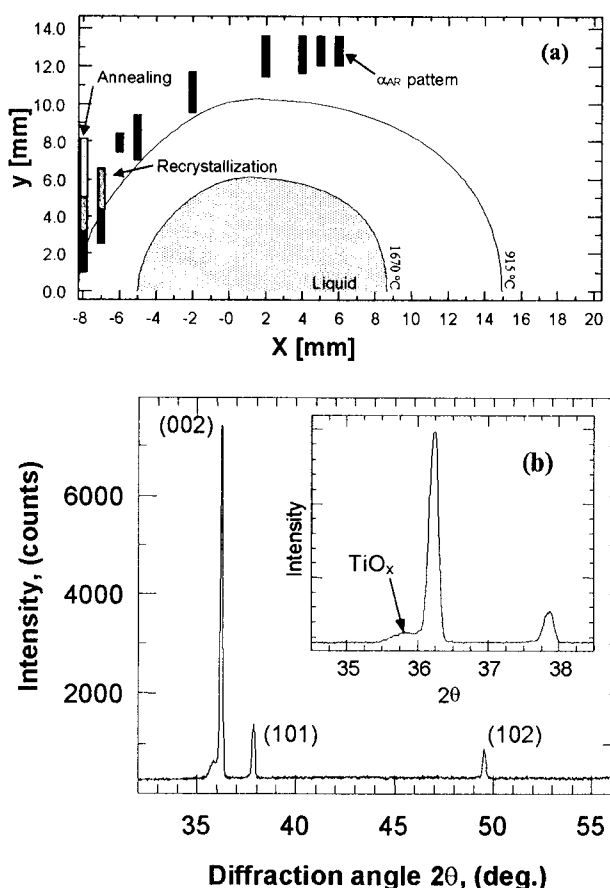


**Figure 9.** (a) SRXRD map highlighting the locations at which the  $\alpha_{AR}$  pattern was observed in the vicinity of the HAZ during welding. Locations in the weld where annealing and recrystallization of the base material can be observed are indicated. (b) The corresponding diffraction pattern. Arrow in the inset indicates a low-angle shoulder due to presence of a hexagonal  $TiO_x$  phase (see text).

Texturing parallel to the hexagonal basal plane leads to an increased (002) intensity compared to the calculated powder pattern for  $\alpha$ -Ti (Figure 2). Stress and disorder result in broad single peaks originating from diffraction domains with sizes on the order of 20 nm. Domain sizes were obtained from the Scherrer formula<sup>14</sup> ( $t = 0.9\lambda/(\nu_{hkl} \cos(\Theta_{hkl}))$ ), with  $t$  the thickness of a diffraction domain,  $\lambda$  the wavelength, and  $\nu_{hkl}$  and  $\Theta_{hkl}$  the peak width (in radians) and Bragg angle of the  $(hkl)$  line, respectively. Due to the instrumental broadening discussed in the "Error Estimates" section, diffraction domain size calculations using the Scherrer formula are not suited to afford absolute values. Thus, diffraction domain sizes were calculated only to compare different phases and evaluate relative microstructural changes, but not to obtain absolute values.

Moving toward the center of the weld in  $x$  and  $y$ , annealing of the base metal takes place with increasing temperature. Defects and stress in the grains are being reduced, and small diffraction domains grow to form larger, more perfect domains. This results in a progressive narrowing of diffraction lines along the positive temperature gradient. Figure 10 shows the variation of the  $\alpha$ -Ti (002) line width for two experimental runs ahead of the weld center at position  $x = -8$  and  $-7$  mm. The  $y$  scales of these two SRXRD runs were combined employing the simplified heat-flow model.<sup>12</sup> Line width narrowing is given as the difference between the width of the  $\alpha_{AR}$  (002) line at temperature and that of the  $\alpha$ -Ti (002) line for the base metal at room temperature. As can be seen from Figure 10, the (002) line width narrowing as a function of  $y$  coordinates along a

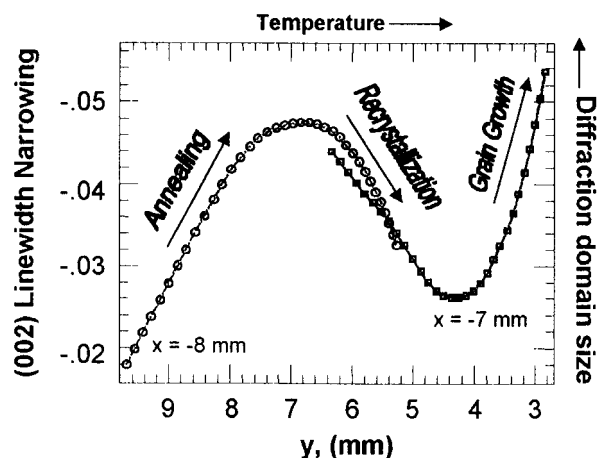


**Figure 10.** Line width narrowing of the  $\alpha$ -Ti(002) peak as a function of  $y$  coordinates along a positive thermal gradient obtained from two SRXRD runs ahead of the weld at positions  $x = -8$  and  $-7$  mm. Plotted is the difference between the width of the  $\alpha_{AR}$ (002) line at temperature and that of the  $\alpha$ -Ti(002) line for the base metal at 20 °C. A large negative difference reflects an increase in diffraction domain size.

positive thermal gradient toward the weld center proceeds via a minimum in domain size. This suggests a three-step mechanism that may be described as follows: (i) an initial annealing of defects and stress in the base metal and growth of diffraction domains resulting in a peak narrowing, (ii) a recrystallization process that yields smaller yet more perfect domains and leads to a broadening of diffraction peaks, and (iii) subsequently a growth of diffraction domains which results in a narrowing of peaks eventually toward the  $\alpha_{RG}$  phase. These three regions are indicated in Figure 9 by different shadings. The observed behavior is in good agreement with the conventional picture of annealing phenomena in metals which is believed to proceed via initial reduction of stress and number of defects, recrystallization, and grain growth. All these steps are evident in the measured diffraction patterns *at temperature*.

In addition to a decrease in peak width in the  $\alpha_{AR}$  pattern along a positive temperature gradient, a distinct shoulder on the low angle side of each  $(hkl)$  line also becomes discernible. This shoulder has previously been identified to be associated with a hexagonal  $TiO_x$  phases that forms on the surface of the titanium metal bar welded in an oxygen ambient.<sup>9</sup> Indeed, a careful profile analysis of the base metal diffraction peaks at room temperature revealed, however, that the  $TiO_x$  shoulder is already present in the initial  $\alpha$ -Ti pattern (Figure 11). Thus, during annealing and recrystallization the  $TiO_x$  shoulder becomes distinguishable due to a combination of line narrowing and peak shifts, while the width and intensity of this shoulder feature remain constant over a large temperature range as shown by invariance of the area under the shoulder in both patterns in Figure 11 ( $\sim 26$  counts $\cdot$ deg). This simply implies the presence of  $TiO_x$  in the base metal (oxygen concentration in base metal is ca. 0.17 wt %) rather than surface oxidation of the material during welding. From the width of the  $TiO_x$  feature, the size of the  $TiO_x$  diffraction domains was calculated to be  $\sim 25$  nm. At higher temperatures ( $T > 700$  °C), the  $TiO_x$  layer seems to grow with rising temperature possibly due to segregation of oxygen to the surface or annealing of  $TiO_x$  domains.

Anisotropy in the thermal expansion coefficients of hcp  $\alpha$ -titanium can be found in different peak shifts of the  $\alpha$ -Ti (101), (002), and (101) diffraction lines.  $\alpha$ -Ti is known to exhibit a larger thermal expansion in the  $c$  direction perpendicular to the basal plane of the hexagonal lattice<sup>17</sup> than in the  $a$  direction. For the  $\alpha$ -Ti (002) peak, for instance, a temperature

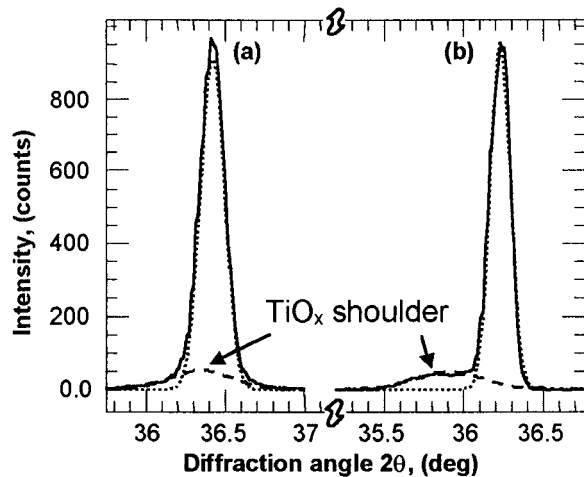


**Figure 11.** Profile analysis of initial base metal  $\alpha$ -Ti pattern at 20 °C (a) compared to an  $\alpha_{AR}$  pattern at ca. 500 °C (b). A low-angle shoulder can be observed in both patterns due to occurrence of  $TiO_x$  in the base metal.

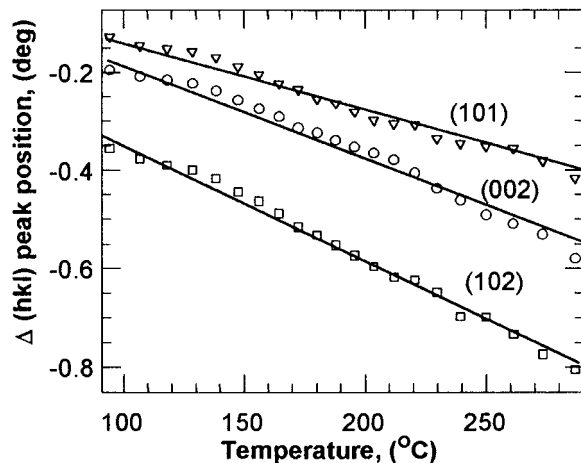


**Figure 12.** Evolution of  $\alpha$ -Ti diffraction peak positions with temperature measured at a position of  $x = 2$  mm with respect to the weld (squares, (102); circles, (002); triangles, (101)). Plotted is the difference  $\Delta(hkl)$  between the  $\alpha_{AR}$  ( $hkl$ ) peak position at temperature and the  $\alpha$ -Ti base metal ( $hkl$ ) peak position at room temperature. Temperature information was extracted from the simplified heat-flow model.

difference of about 200 K should result in a peak shift of about  $0.06^\circ$  in  $2\theta$  for the scattering geometry used (thermal expansion coefficient  $C_a = 7.5 \times 10^{-6} \text{ K}^{-1}$  in the  $a$  direction and  $C_c = 1.1 \times 10^{-5} \text{ K}^{-1}$  in the  $c$  direction<sup>17</sup> yield  $C_{(002)} = 3.0 \times 10^{-40} (2\theta)/\text{K}$  for (002) line). Calculation of relative diffraction plane  $d$  spacing expansion for the three  $\alpha$ -Ti (101, 002, 102) peaks seen in the SRXRD data yields the largest effect on the (102) diffraction peak ( $C_{(101)} < C_{(002)} < C_{(102)}$ , with  $C_{(102)}$  being  $\sim 20\%$  more than  $C_{(002)}$  and  $\sim 30\%$  more than  $C_{(101)}$ ). Figure 12 shows the peak shift of the three ( $hkl$ )  $\alpha$ -Ti peaks with temperature for an experimental SRXRD run at a position of  $x = -2$  with respect to the weld center. ( $hkl$ ) peak positions were determined from a least-squares fit of a Gaussian profile function to the individual diffraction peaks. Temperature data were taken from the simplified heat-flow model. For clarification, the difference of ( $hkl$ ) peak positions at elevated temperature and at room temperature is displayed. Different expansion coefficients  $C_{(hkl)}$  for different directions in the  $\alpha$ -Ti lattice (Figure 12) can be seen from different slopes of the corresponding curves. A linear fit to each curve in Figure 12 yields expansion coefficients in terms of diffraction angle  $2\theta$  of  $C_{(002)} = 2.0 \times 10^{-30} (2\theta)/\text{K}$ ,  $C_{(101)} = 1.5 \times 10^{-30} (2\theta)/\text{K}$ , and  $C_{(102)} = 2.5 \times$

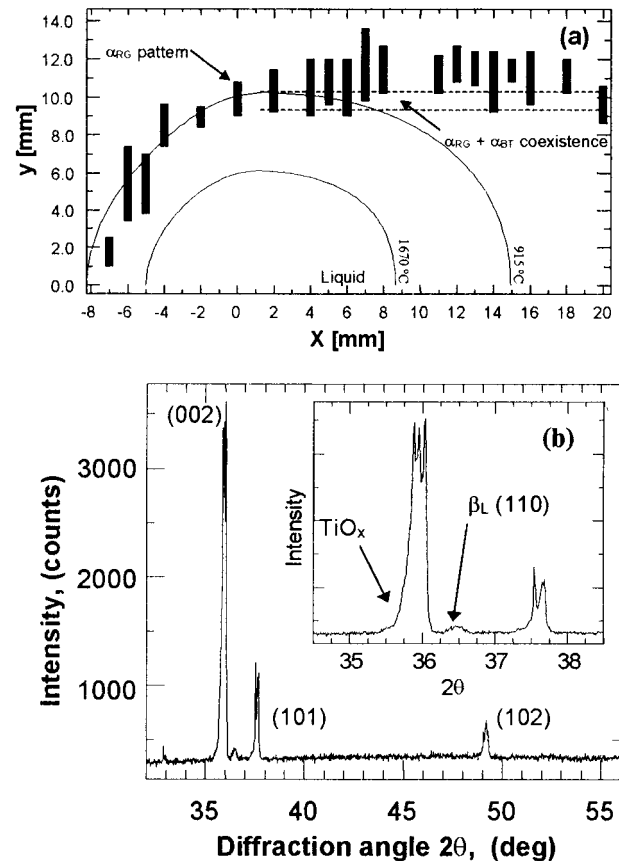


**Figure 13.** (a) SRXRD map highlighting the locations at which the  $\alpha_{RG}$  pattern was observed in the vicinity of the HAZ during welding. Black bars inside the HAZ denotes regions of  $\alpha + \beta$  coexistence. Dotted line indicates  $\alpha_{RG}$  and  $\alpha_{BT}$  coexistence zone (see text). (b) The corresponding diffraction pattern. Inset shows an enhanced  $TiO_x$  shoulder together with a  $\beta_L$  (110) peak due to contribution of  $\beta$ -Ti.

$10^{-30} (2\theta)/\text{K}$ . The qualitative difference between the  $C_{(hkl)}$  expansion coefficients is in agreement with the above-mentioned considerations ( $C_{(101)} < C_{(002)} < C_{(102)}$ ), with the ratio between  $C_{(101)}$  and  $C_{(102)}$  of 0.6 being slightly higher than the calculated difference of  $\sim 30\%$ . Furthermore, the experimental absolute values exceed the expected ones by about an order of magnitude. This might be due to an additional peak shift caused by a slight wobbling motion of the titanium bar during the experiment as described in the "Error Estimates" section. Similar to the footprint effect, this motion will have a stronger effect on high angle diffraction peak and would explain the observed discrepancies. A further quantitative analysis of peak position and peak shift is rendered difficult under these circumstances and was not attempted.

**The  $\alpha_{RG}$  Pattern: Location and Associated Microstructure.** The locations at which the  $\alpha_{RG}$  pattern was observed are plotted in Figure 13a. The corresponding diffraction pattern is shown in Figure 13b. Further annealing and growth of  $\alpha$ -Ti diffraction domains are expected with increasing temperature toward the weld center. The process can indeed be observed as a continuous decrease in diffraction peak width, which eventually leads to a transition from  $\alpha_{AR}$  to  $\alpha_{RG}$  patterns.  $\alpha$ -Ti diffraction patterns from inside the HAZ (915 °C isotherm) correspond to  $\alpha + \beta$  coexistence regions. Different kinetic mechanisms that govern  $\alpha \rightarrow \beta$  and  $\beta \rightarrow \alpha$  phase transformation ahead and behind the center of the weld, respectively, are responsible for the occurrence of  $\alpha$ -Ti above the phase transformation isotherm on the heating side of the weld.<sup>12</sup>

Although the  $\alpha_{RG}$  pattern does not denote a distinct new  $\alpha$ -Ti



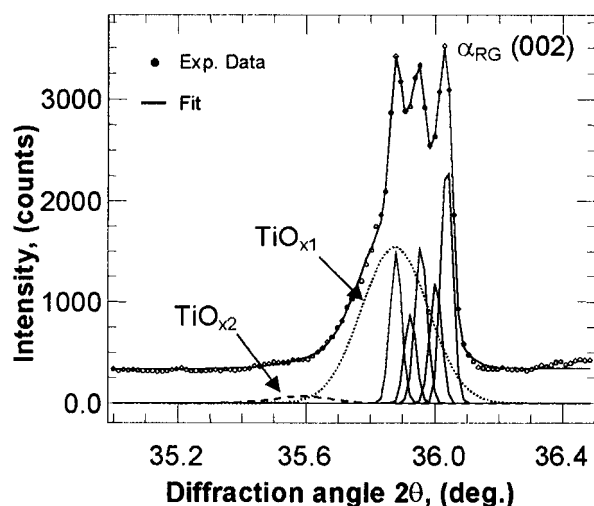


**Figure 14.** Profile refinement of  $\alpha$ -Ti (002) peak in an  $\alpha_{RG}$  diffraction pattern. Splitting of a single (002) Bragg peak is due to the scattering geometry used. Additional contribution of two different  $TiO_x$  phases to a low-angle shoulder is indicated. The five narrow peaks (with same refined peak width) are attributed to at least five large domains in  $\alpha$ -Ti diffracting into the photodiode.

microstructure, the splitting of single Bragg diffraction peak into multiplets (Figure 13b) requires some explanations. Scattering geometry consideration discussed earlier in the "Error Estimates" section (Figure 4) revealed that the appearance of more than one peak in a single Bragg diffraction line does not indicate a discontinuous change in lattice spacing and coexistence of slightly different  $\alpha$ -Ti lattices, but has its origin in the X-ray beam footprint on the metal bar. Taking into account the probed volume on the titanium metal bar and the angle of acceptance on the metal bar (Figure 4) and on the detector, and assuming a domain size of about  $3\ \mu\text{m}$ , the number of diffraction domains fulfilling Bragg's law in one 6 s scan can be estimated to be on the order of 10. Therefore, single "spikes" in a diffraction peak correspond to single large diffraction domains that diffract the X-ray beam to a slightly different position on the photodiode array (Figure 4). The size of the footprint and maximum spacing of single peaks within the experimental (002) diffraction line corroborates this assumption. Similar to the  $\alpha_{AR}$  pattern, the observed  $\alpha_{RG}$  pattern also exhibits a strong (002) intensity due to texture of the base metal and a low-angle shoulder due to contribution of  $TiO_x$  phases. However, the integrated intensity of the  $TiO_x$  peak seems to be larger for  $\alpha_{RG}$  patterns compared to the base metal. Two reasons can account for this observation. First, diffusion and segregation of oxygen into the existing  $TiO_x$  layer and annealing of the same might result in an increase of  $TiO_x$  peak intensity. Second, in the coexistence region with  $\beta$ -Ti (Figure 13), oxygen from titanium particles that already have been transformed to  $\beta$ -Ti diffuses to the remaining  $\alpha$ -Ti, which has a higher oxygen solubility, resulting in an increase of the  $TiO_x$  contribution to the  $\alpha$ -Ti diffraction peaks. Additionally, a distinction of  $TiO_{x1}$  and  $TiO_{x2}$  diffraction peaks (Figure 14) as previously reported<sup>9</sup> is possible at this state of annealing and grain growth of  $\alpha$ -Ti. An  $\alpha_{RG}$  diffraction domain thickness of about 300 nm was estimated from single "spike" width obtained from a least-squares fit of several Gaussian functions to one Bragg peak (Figure 14). Due to the limited number of data points, peak widths (five in number) were refined to vary the same plus two extra peaks for  $TiO_{x1}$  and  $TiO_{x2}$  shoulders.

**The  $\beta$  and  $\beta_L$  Patterns: Location and Associated Microstructure.** The locations at which the  $\beta$  and  $\beta_L$  pattern were

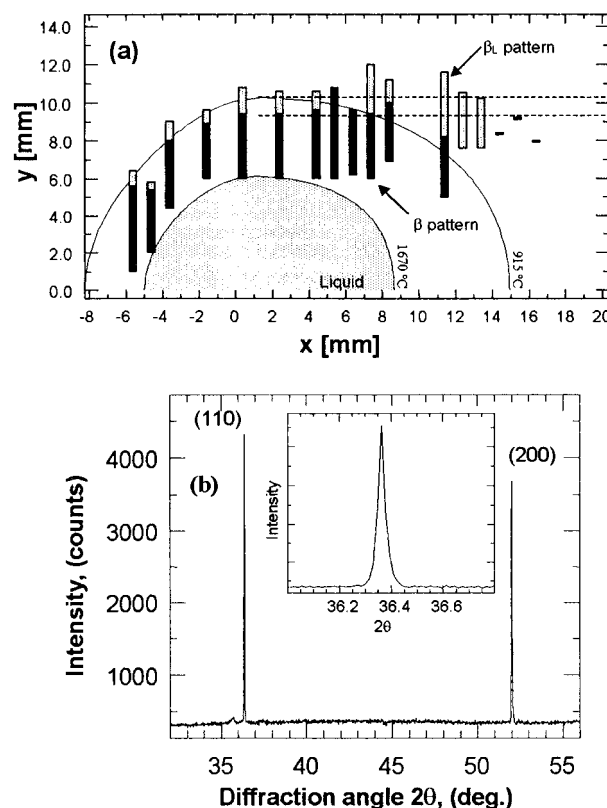


**Figure 15.** (a) SRXRD map highlighting the locations at which the  $\beta$  and  $\beta_L$  pattern was observed in the vicinity of the HAZ during welding. (b) The corresponding  $\beta$ -Ti diffraction pattern.

observed are plotted in Figure 15a. The corresponding diffraction pattern is shown in Figure 15b. At temperatures above the  $915\ ^\circ\text{C}$   $\alpha \rightarrow \beta$  phase transformation isotherm  $\beta$ -Ti becomes the thermodynamically more stable titanium phase. In the vicinity  $\sim 2.0$  mm of the liquid weld pool and on the backside of the HAZ, "pure"  $\beta$ -Ti diffraction patterns are observed (Figure 15). Further out in the colder region but still in the HAZ, a large coexistence region with  $\alpha$ -Ti can be found ahead of the liquid weld pool (Figure 7), whereas this region appears to narrow with  $x$ . The transformation kinetics (hence mechanism) on the leading side of the liquid pool with thermal gradients  $\sim 100\ \text{K/mm}$  may be very different from that of the backside having a lower thermal gradient. Such difference in kinetics is largely responsible for the variation in spatial extent of the  $\alpha + \beta$  coexistence regions in the HAZ.<sup>12</sup>

Large  $\beta$ -Ti diffraction domains in the hot region of the HAZ lead to strong and very narrow diffraction peaks (Figure 15b). Again, splitting within a given diffraction peak similar to those discussed for the  $\alpha_{RG}$  pattern is observed. Since the  $\beta$ -Ti grains seem to grow larger than  $\alpha$ -Ti grains particularly in the hot region of the HAZ near the weld pool, generally only one or two "spikes" can be observed with an occasionally missing of all diffraction peaks. Similar to the base metal  $\alpha$ -Ti patterns, the  $\beta$ -Ti patterns also show a preferred orientation in the diffraction patterns. On the average, most patterns showing a strong (110) peak and only a small or no (200) peak can be found in the experimental data. This might be inherited from the preferred orientation of the  $\alpha$ -Ti phase in (002) direction. In the  $\alpha \rightarrow \beta$  phase transformation the most densely packed hcp layer (basal plane (002)) in  $\alpha$ -titanium becomes the most densely packed layer in the  $\beta$ -titanium bcc structure leading to a preferred orientation of large  $\beta$  grains in the (110) direction of the cubic  $\beta$ -Ti lattice. Furthermore, the size of  $\beta$  diffraction

domains in the colder part of the HAZ right after the phase transformation has taken place amounts to ca. 300 nm as calculated from the diffraction peak width obtained from profile refinement to a multiplet (200) peak. This value is in good agreement with the diffraction domain size of  $\alpha_{RG}$ -Ti prior to phase transformation and substantiates the fact that the entire  $\alpha$ -Ti grain transforms to  $\beta$ -Ti and retains its grain size upon phase transformation. This corroborates the idea of maintaining the most dense layer in hcp  $\alpha$ -Ti and bcc  $\beta$ -Ti upon transformation as cause for the observed texture in  $\beta$ -Ti.

Besides diffraction patterns exhibiting strong  $\beta$ -Ti peaks, a low-intensity (110)  $\beta_L$  peak is also observed usually in coexistence with the  $\alpha_{RG}$  pattern (Figure 13). The  $\beta_L$  pattern extends over a considerably long range in the  $y$  direction. The underlying microstructures that belong to locations on the map showing  $\beta_L$  diffraction patterns have to be divided into two different phases. Diffraction data taken below a straight line drawn from the maximum of the 915 °C isotherm in  $y$  parallel to  $x$  (Figure 15) belong to residual  $\beta$ -Ti that was not completely back-transformed to  $\alpha$ -Ti. This residual  $\beta$ -Ti stems from the region in the HAZ where the phase transformation temperature was exceeded. The ratio of integrated intensities of (110)  $\beta_L$  peak and (002)  $\alpha_{BT}$  peak amounts to ca. 0.1. In contrast, (110)  $\beta_L$  peaks measured above the maximum of the 915 °C isotherm in  $y$  correspond to  $\alpha$ -Ti that had already started to but did not completely transform to  $\beta$ -Ti. The early onset of the transformation can be explained by a slightly lowered  $\alpha \rightarrow \beta$  transformation temperature in the vicinity of bcc nucleation sites within the material or due to impurities in the titanium.<sup>12</sup>

**The  $\alpha_{BT}$  Pattern: Location and Associated Microstructure.** The locations at which the  $\alpha_{BT}$  pattern was observed are plotted in Figure 16a. The corresponding diffraction pattern is shown in Figure 16b. This new  $\alpha_{BT}$  pattern is found behind the “ $\beta$ -pattern” region and outside the HAZ (Figure 16) and is associated with a new microstructure of  $\alpha$ -Ti. This pattern corresponds to  $\alpha$ -Ti that has been back-transformed from  $\beta$ -Ti formed in the HAZ around the weld. Compared to the  $\alpha_{RG}$  and the  $\beta$  pattern, the  $\alpha_{BT}$  pattern in Figure 16 shows no multiple diffraction line, and the line width is in the same range as the  $\alpha_{AR}$  pattern (Table 1). The size of  $\alpha_{BT}$  phase diffraction domains amounts to about 100 nm as obtained from the Scherrer formula. Since the  $\alpha_{BT}$  phase stems from large  $\beta$  grains in the HAZ, it implies that the size of the  $\beta$ -Ti diffraction domains is *not* retained upon back-transformation to  $\alpha$ -Ti. This in turn suggests that large  $\beta$  domains break up into smaller  $\alpha$ -Ti domains during the back-transformation.

Figure 17 shows a series of SRXRD diffraction patterns measured along the  $y$  direction at  $x = 15$  mm behind the weld. A transition can be seen at about  $y = 10$  mm from diffraction patterns showing a (101) preference to the base metal type patterns with a strong (002) peak. This indicates a certain texture in the back-transformed  $\alpha$ -Ti inherited from the preferred (110) orientation of the  $\beta$ -Ti phase in the HAZ. However, occasionally  $\alpha_{BT}$  patterns show the  $\alpha$ -Ti (100) and (110) peaks that are not observed in the base metal pattern, and only very few patterns show all five hcp  $\alpha$ -Ti peaks calculated for the  $\alpha$ -Ti powder pattern (Figure 2a). If during  $\beta \rightarrow \alpha$  back-transformation the most dense lattice planes in  $\beta$ -Ti were to become the most dense layer in  $\alpha$ -Ti, a (002) preferred orientation in the metal would result. This, however, is not observed experimentally. The reason for this effect is not clear at the moment.<sup>18,19</sup>

Another characteristic of the  $\alpha_{BT}$  pattern is the absence of a distinct low-angle shoulder due to contributions of  $TiO_x$ . This

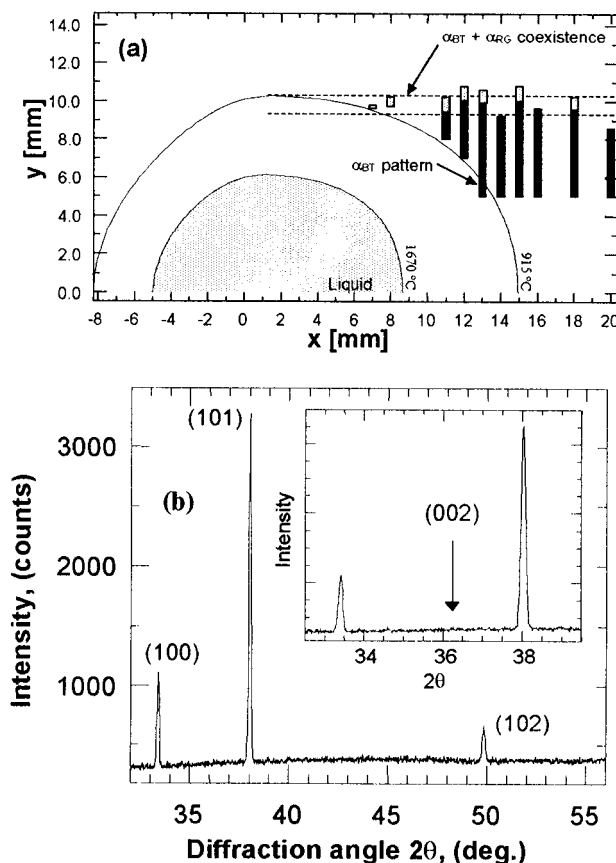


**Figure 16.** (a) SRXRD map highlighting the locations at which the  $\alpha_{BT}$  pattern was observed in the vicinity of the HAZ during welding. (b) The corresponding diffraction pattern. Arrow in inset indicates absence of  $\alpha$ -Ti (002) peak in this pattern.

corroborates the assumption of  $TiO_x$  diffraction peaks originating from surface oxidized base metal or oxygen impurities rather than oxidation of the metal during welding. The  $\alpha \rightarrow \beta$  phase transformation results in oxygen diffusion from the forming  $\beta$ -Ti grains to remaining  $\alpha$ -Ti base metal grains owing to a higher solubility of oxygen in  $\alpha$ -Ti. Therefore,  $\beta \rightarrow \alpha$  back-transformation affords low oxygen  $\alpha$ -Ti that shows no distinct contribution of  $TiO_x$ . Furthermore, the transition from  $\alpha_{BT}$  to  $\alpha_{RG}$  patterns exhibits a  $\alpha_{BT} + \alpha_{RG}$  coexistence region at the boundary between the two microstructures (Figure 17). This region stems from the  $\alpha + \beta$  coexistence region in the HAZ ( $y = 9$ – $10$  mm) that results in a mixed zone upon  $\beta \rightarrow \alpha$  back-transformation containing  $\alpha$ -Ti that has never been transformed to  $\beta$ -Ti and back-transformed  $\alpha$ -Ti. Diffraction patterns belonging to this coexistence region can be identified by the occurrence of a low-angle  $TiO_x$  shoulder together with a distinct (101) preferred orientation and the presence of (100) and (110)  $\alpha$ -Ti peaks. Figure 18 shows a comparison of a  $\alpha_{BT}$  diffraction pattern and a coexistence pattern. A low-angle shoulder can be seen at the (002) peak of the coexistence pattern, whereas the strong (101) peak in both the coexistence and the  $\alpha_{BT}$  pattern exhibits a symmetric profile without a low-angle shoulder. Additionally, the  $\alpha_{BT}$  pattern exhibits low  $\beta$  (110) peak due to residual amounts of  $\beta$ -Ti behind the HAZ of the weld.

### Concluding Remarks

In this paper we have described a refined version of our SRXRD technique<sup>8,9</sup> using an intense synchrotron beam emitted from a multipole wiggler at Stanford Synchrotron Radiation Laboratory and, as a case study, applied it to study in some

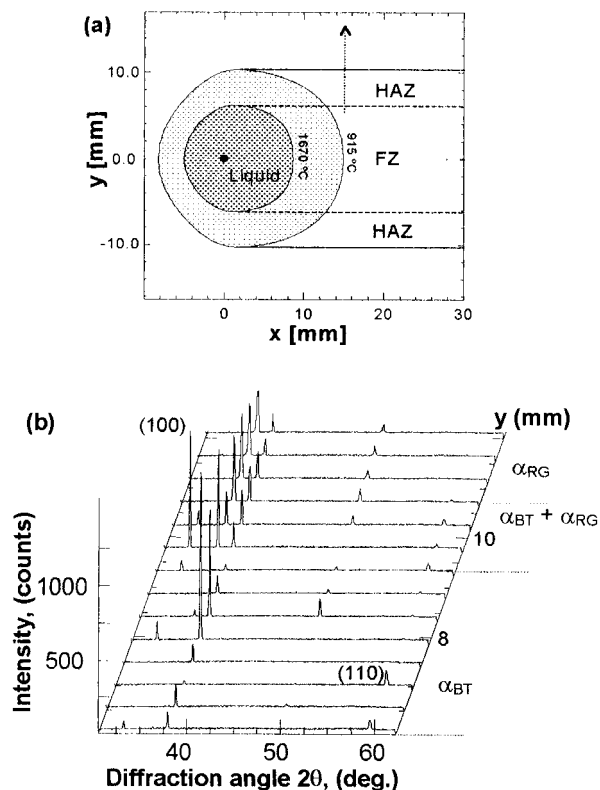


**Figure 17.** Evolution of X-ray diffraction patterns measured across the HAZ boundary in the  $y$  direction at a position  $x = 15$  mm behind the center of the weld indicating  $\alpha_{BT}$  and  $\alpha_{RG}$  regions as well as  $\alpha_{BT} + \alpha_{RG}$  coexistence.

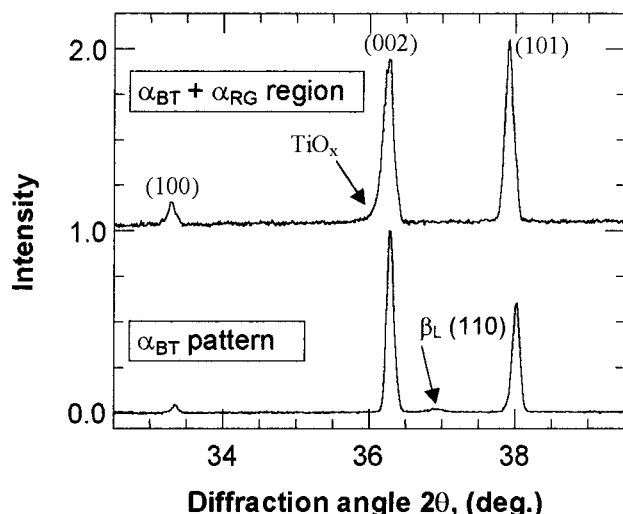


**Figure 18.** Comparison of  $\alpha_{BT}$  pattern from  $\alpha$ -Ti back-transformed from HAZ  $\beta$ -Ti and a pattern from the boundary between  $\alpha_{BT} + \alpha_{RG}$  regions. Indicated by arrows are residual amounts of  $\beta$ -Ti ( $\beta_L$  (110)) in the  $\alpha_{BT}$  pattern and a low-angle shoulder due to  $TiO_x$  contribution to  $\alpha_{RG}$  pattern. (Note the rare occasion of a strong (002) line in a  $\alpha_{BT}$  pattern (Figure 17).)

detail the phase distribution and phase transformation in a highly nonisothermal process. The experimental results presented here for Ti fusion welds clearly illustrate the novelty and usefulness of this tool to map solid-state phases and their boundaries in situ with submillimeter spatial resolution ( $\sim 200 \mu\text{m}$ ) during materials processing at temperature and in real time.

In commercially pure grade 2 titanium employed in this work, an allotropic transformation from a hcp  $\alpha$ -phase to a bcc  $\beta$ -phase at  $\sim 915^\circ\text{C}$  occurs in the solid state. Detailed profile analysis

of the SRXRD patterns collected as a function of position for a 1.9 kW Ti fusion weld moving at 1.1 mm/s revealed a number of high-temperature microstructural regions in the vicinity of the HAZ around the liquid weld pool: (i) Observed variation of the Bragg line width shows that the continuous microstructural evolution of the base metal along a positive thermal gradient from room temperature to the  $\alpha \rightarrow \beta$  transformation isotherm follows a three-step process of annealing, recrystallization, and grain growth. (ii) Inside the HAZ within  $\sim 1$  mm of the  $915^\circ\text{C}$  isotherm, a region of  $\alpha + \beta$  coexistence occurs, indicative of only a partial  $\alpha \rightarrow \beta$  transformation due to kinetic effects.<sup>12</sup> (iii) Further within the HAZ toward the weld pool, where the thermal gradient is steepest, a completely transformed  $\beta$ -Ti region is located. The preferred orientation of the transformed  $\beta$ -phase is found inherited from texture in the base metal and corroborates that the most dense lattice plane in  $\alpha$ -Ti remains to be the most dense  $\beta$ -Ti plane upon transformation. (iv) The back-transformed  $\alpha$ -Ti behind the weld results in smaller diffraction domains that exhibit, however, a different texture than that of the base metal. In general, the observed phase distribution and boundaries are in good agreement with the transformation isotherms calculated from a simple heat-flow model.

Spatially resolved and dynamic structural information on this sort, not readily obtainable with either conventional structural techniques (due to their ex-situ and post-mortem nature) or simple heat-flow calculations, must be taken into account for qualitative understanding and quantitative modeling of phase transformation kinetics and microstructural evolution in systems under highly nonisothermal conditions. Our instrumentation may further be improved to enable extraction of more information from the SRXRD data. For instance, by mechanically stabilizing the sample geometry in reducing unwanted wobbling motions, reliable peak shifts can be obtained to correlate with tabulated thermal expansion coefficients to derive temperature information at various spatial locations of interest. The temperature data can then be used as input parameters in theoretical analysis for more realistic modeling of phase boundaries and associated transformation kinetics. Moreover, with high brightness beams available at third generation synchrotron sources, spatial resolution down to  $1 \mu\text{m}$  and better may be enhanced without sacrificing flux on sample.

**Acknowledgment.** This work was performed under the auspices of the U.S. Department of Energy (DOE), Lawrence Livermore National Laboratory, under Contract W-7405-ENG-48. T.R. is grateful to the Alexander von Humboldt Foundation, Germany, for a Feodor Lynen Research Fellowship. The synchrotron experiments were carried out at Stanford Synchrotron Radiation Laboratory supported by DOE, Division of Chemical Sciences.

## References and Notes

- (1) *International Trends in Welding Science and Technology*; David, S. A., Vitek, J. M., Eds.; ASM International: Materials Park, OH, 1993.
- (2) Damkroger, B. K.; Edwards, G. R.; Rath, B. B. *Welding J.* **1989**, *68*, 290.
- (3) McGuire, M. C.; Santella, M. L.; Damkroger, B. K. *The Science of Metal Joining*; Cieslak, M. H., Perepezko, J., Kang, S., Glicksman, M. E., Eds.; TMS: 1992; p 41.
- (4) Wong, J.; Larson, M.; Holt, J. B.; Waide, P. A.; Rupp, B.; Frahm, R. *Science* **1990**, *249*, 1406.
- (5) Frahm, R.; Wong, J.; Holt, J. B.; Larson, E. M.; Rupp, B.; Waide, P. A. *Phys. Rev. B* **1992**, *46*, 9205.
- (6) Larson, E. M.; Wong, J.; Holt, J. B.; Waide, P. A.; Rupp, B.; Terminello, L. J. *J. Mater. Res.* **1993**, *8*, 1533.



- (7) Rupp, R.; Wong, J.; Holt, J. B.; Waide, P. A. *J. Alloys Compds.* **1994**, 209, 25.
- (8) Elmer, J. W.; Wong, J.; Fröba, M.; Waide, P. A.; Larson, E. M. *Met. Mater. Trans.* **1996**, 27A, 775.
- (9) Wong, J.; Fröba, M.; Elmer, J. W.; Waide, P. A.; Larson, E. M. *J. Mater. Science.* **1997**, 32, 1493.
- (10) Karpenko, V.; Kinney, J. H.; Kulkarni, S.; Neufeld, K.; Poppe, C.; Tirsell, K. G.; Wong, J.; Cerino, J.; Troxel, T.; Yang, J.; Hoyer, E.; Green, M.; Humpries, D.; Marks, S.; Plate, D. *Rev. Sci. Instrum.* **1989**, 60, 1451.
- (11) Larson, E. M.; Waide, P. A.; Wong, J. *Rev. Sci. Instrum.* **1991**, 62, 53.
- (12) Elmer, J. W.; Wong, J.; Ressler, T. *Met. Mater. Trans.* **1998**, 29A, 2761.
- (13) Ressler, T. *J. Phys. IV* **1997**, 7 (C2), 269.
- (14) Cullity, D. *Elements of X-ray Diffraction*, 3rd ed.; Addison and Wesley: New York, 1967.
- (15) Donachie, M. *Titanium A Technical Guide*: ASM International: Materials Park, OH, 1989.
- (16) LAZY Scientific Software, PhysiSoft Corporation, Wilmington, DE.
- (17) Schmitz-Pranghe, N.; Dünner, P. *Z. Metall.* **1968**, 59, 377.
- (18) Glen, J. W.; Pugh, S. F. *Acta Metall.* **1954**, 2, 520.
- (19) Zhu, Z. S.; Gu, J. L.; Chen, N. P. *Scr. Metall. Mater.* **1994**, 30, 605.